Electrochimica Acta 269 (2018) 102–110

Contents lists available at ScienceDirect

Electrochimica Acta

journal homepage: www.elsevier.com/locate/electacta

Synthesis of self-assembly 3D porous $Ni(OH)_2$ with high capacitance for hybrid supercapacitors

Fangyan Liu, Xiang Chu, Haitao Zhang, Binbin Zhang, Hai Su, Long Jin, Zixing Wang, Haichao Huang, Weiqing Yang*

State Key Laboratory of Traction Power, Key Laboratory of Advanced Technologies of Materials (Ministry of Education), School of Materials Science and Engineering, Southwest Jiaotong University, Chengdu, 610031, China

ARTICLE INFO

Article history:
Received 14 November 2017
Received in revised form
14 January 2018
Accepted 24 February 2018
Available online 2 March 2018

Keywords:
Nickel hydroxide
Self-assembly
Porous structure
Electrochemical performance
Hybrid supercapacitors

ABSTRACT

Nickel hydroxide has shown extraordinary promise for hybrid supercapacitors because of the high theoretical capacity and low cost, but is usually limited by its low power density and complex synthetic process. Here, we report the design of a self-assembly three-dimensional (3D) porous $Ni(OH)_2$ for high-performance energy storage through a simple, cost-effective, and environmentally friendly solvothermal-precipitation method. The 3D structure with interconnected network provides superior electron transportation properties, and the hierarchical porous architecture facilitates quick ion diffusion. The $Ni(OH)_2$ obtained at 250 °C delivers a high capacitance of 2110 F g^{-1} at 1.0 A g^{-1} and a moderate cycling stability with 53% of the maximum specific capacitance over 2000 cycles at 5.0 A g^{-1}. Additionally, on integration of the prepared $Ni(OH)_2$ with hierarchically porous carbons as negative electrode material, the hybrid supercapacitor device delivers a high capacitance of 115 F g^{-1} and a high energy density of 40.9 W h kg^{-1} at a power density of 405 W kg^{-1}. This study not only provides a simply controllable growth method of the unique self-assembly 3D porous $Ni(OH)_2$ with high performance but also opens up a new approach to prepare various metallic oxides/hydroxides with excellent performance for highly promising practical energy-storage systems.

© 2018 Elsevier Ltd. All rights reserved.

1. Introduction

The increasing acute global energy crisis and the ever-increasing energy needs have driven the progress of the high-performance energy storage and conversion devices. As a powerful and efficient electrochemical energy storage system, electrochemical supercapacitors have received growing interest over the past decades in virtue of their distinct superiorities of high power density, fast charging/discharging rate, long cycling life, easy fabrication, and environmental benignity [1,2]. Hybrid supercapacitors typically compose of a battery-type electrode and a supercapacitor-type electrode, for instance, AC//$Li_4Ti_5O_{12}$, AC//$Ni(OH)_2$, AC//graphite, AC//$LiMn_2O_4$, and AC//PbO_2 [2,3]. As an important component of capacitor system, hybrid supercapacitors have been used in an extensive range of practical and significant applications, such as the renewable energies, hybrid electric vehicles, and all-electric vehicles [3]. Among these practical applications, the electrochemical performances of electroactive materials undoubtedly act a pivotal role in the overall electrochemical performances of energy storage systems [4].

Because of its low cost, abundant reserve, and promising electrochemical property [5,6], nickel hydroxide ($Ni(OH)_2$), regarded as a typical battery-type electrode material, has gained considerable attention and been extensively applied as electrode material for not only commercial Ni–MH or Ni–Cd batteries but also hybrid supercapacitors [3,7]. Nickel hydroxide with hexagonal-layered structure has two common polymorphs, α-$Ni(OH)_2$ and β-$Ni(OH)_2$ [6,8]. Because of its instability under strong alkaline solution, α-$Ni(OH)_2$ rapidly transforms into β-$Ni(OH)_2$, which restricts its practical application [8,9]. In contrast, β-$Ni(OH)_2$ possesses the better stability than α-$Ni(OH)_2$, and has been applied extensively as the positive electrode material. More than that, numerous studies have demonstrated that the electrochemical properties of electrode materials not only heavily rely on crystal structure but also the

* Corresponding author. Key Laboratory of Advanced Technologies of Materials (Ministry of Education), School of Materials Science and Engineering, Southwest Jiaotong University, No. 111, North 1st Section of Second Ring Road, Jinniu District, Chengdu, 610031, China.
E-mail address: wqyang@swjtu.edu.cn (W. Yang).

https://doi.org/10.1016/j.electacta.2018.02.130
0013-4686/© 2018 Elsevier Ltd. All rights reserved.

morphology and specific surface area [9]. To achieve ideal electrochemical property of the nickel hydroxide, an ingenious structure and morphology of pure $Ni(OH)_2$ with high surface area is highly desired. A lot of efforts have been devoted to obtain various morphologies and structures of nickel hydroxide, including zero-dimensional (nanoparticles [10]), one-dimensional (nanowires [11]), two-dimensional (nanosheets [12–14], nanowalls [15], nanoplates [16], and nanoflakes [17,18]), and three-dimensional structures (hollow microspheres [6] and flower-like structure [2]). Compared with the low-dimensional structure materials, 3D structure materials usually possess high specific surface areas, open porous structures, and/or highly crystalline film-like flakes, which are beneficial for enlarging the contact area between electrolyte and electrode, increasing the electrochemically reactive sites, and shortening the ion and electron transportation pathways, which make them ideal candidates for the fabrication of high-performance energy storage devices. So far, many approaches have been adopted to prepare the three-dimensional nano- and micro-structural nickel hydroxide, including electrochemical deposition [19], chemical precipitation, and template approaches [20]. However, all the above-mentioned methods are complex, difficult to control, and hard to make large-scale preparation. Therefore, it is extremely necessary to develop new and simple methods under mild conditions for the large-scale controllable preparation of three-dimensional structural $Ni(OH)_2$. Furthermore, the low-dimensional building blocks self-assembling into 3D structures of $Ni(OH)_2$ has elicited much interest because of the gentle synthesis conditions [6].

In this paper, we creatively design a novel solvothermal-precipitation route for the successful preparation of the self-assembly 3D porous $Ni(OH)_2$. This proposed approach is relatively facile, cost-effective, eco-friendly, and mild-solution processed for the homogeneous synthesis of $Ni(OH)_2$, therefore, it acquires a promising expectation in industrial production. A combined features of high specific surface area and hierarchical porous architecture are acquired in this obtained $Ni(OH)_2$. Importantly, this simple method yielded $Ni(OH)_2$ microflowers have a specific capacitance of 2110 F g^{-1} at the current density of 1.0 A g^{-1} and show great potential application in hybrid supercapacitors; the device with $Ni(OH)_2$ as positive electrode and hierarchically porous carbon as negative electrode delivers a specific capacitance of 115 F g^{-1} and an energy density of 40.9 W h kg^{-1} at the power density of 405 W kg^{-1}. We are optimistic that this novel solvothermal-precipitation method can be applied to other metallic oxides/hydroxides for their applications in highly promising energy-storage systems.

2. Experimental

2.1. Synthesis of self-assembly 3D porous $Ni(OH)_2$

In this work, all chemicals are of analytical grade and utilized as received without further purification. Nickel acetate tetrahydrate ($Ni(CH_3COO)_2 \cdot 4H_2O$, 99.0%) was bought from Aladdin Industrial Corporation. Ethanol (C_2H_5OH, 99.7%) and urea ($CO(NH_2)_2$, 99.0%) were bought from Chengdu Kelon Chemical Reagent Factory.

The solution-based solvothermal-precipitation approach is applied to synthesize the $Ni(OH)_2$ and the detailed synthetic process is illustrated schematically in Fig. 1a. In this typical synthesis protocol, 0.625 g $Ni(CH_3COO)_2 \cdot 4H_2O$ and 1.5 g $CO(NH_2)_2$ were added into in 30 mL ethanol and keeping stirring until all chemicals were almost dissolved. Then, the obtained precursor solution was moved to a 50 mL autoclave which was heated at 160 °C for 2 h. It was found that the obtained product was just the blue liquid without solid product. Then, the blue liquid was poured into a beaker along with adding a large amount of deionized water. It was

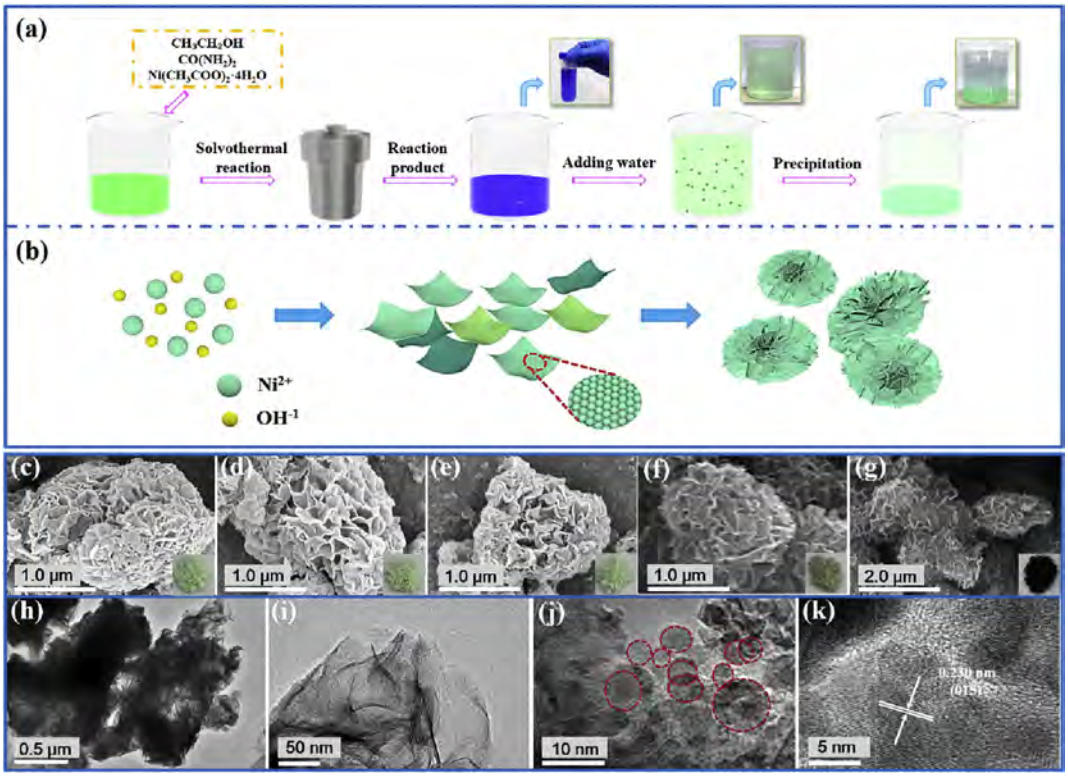

Fig. 1. (a) Experimental procedure and (b) schematic of formation process of the self-assembly 3D porous $Ni(OH)_2$; SEM images of (c) Sample-100, (d) Sample-150, (e) Sample-200, (f) Sample-250, and (g) Sample-300 (the digital photographs at the lower right corner are the pictures of real products); (h, i, j) TEM images and (k) HRTEM image of Sample-100.

found that there were many light green products gradually coming into being. After 48 h, the product was collected by centrifugation and washed several times with deionized water, then dried in an oven overnight at 100 °C, after that, heated to 150, 200, 250, and 300 °C with a heating rate of 1 °C min^{-1} and kept for 30 min in air. The products obtained under different conditions were named Sample-100, Sample-150, Sample-200, Sample-250, and Sample-300, respectively.

2.2. Characterizations

A field-emission scanning electron microscopy (FESEM) (JEOL, JSM-7001 F) was adopted to characterize the structure and morphology of the products. Transmission electron microscopy (TEM) and high-resolution TEM (HRTEM) were carried out on a JEOL JSM- 2100 F operating at an accelerating voltage of 200 kV. The XPert Pro MPD (Holland) X-ray diffractmeter with Cu K_a radiation ($\lambda = 0.154$ nm) was used to obtain the X-Ray diffraction (XRD) patterns which were recorded in the 2θ range of 10–80° with the step size of 0.04°. Fourier-Transform Infrared (FTIR) spectra of the product was performed with a Fourier transform infrared (FTIR) instrument (Magna 560, Nicolet, Thermo Electron Corp., USA). The sample was investigated in the wavenumber range of 400–4000 cm^{-1} using 32 scans with a spectral resolution of 4 cm^{-1}. The chemical status of the sample was determined by an X-ray photoelectron spectroscopy (XPS, Thermo Fisher ESCALAB 250Xi) with monochromatic Al Kα as the excitation source. N_2 adsorption/desorption isotherms at 77 K were obtained with the aid of Quantachrome 2SI-MP-9 surface area and pore size analyzer, and the specific surface areas of the products were evaluated by Brunauer-Emmett-Teller (BET) method while the pore size distributions were measured according to the density functional theory (DFT).

2.3. Electrochemical measurements

The electrochemical properties of the $Ni(OH)_2$ samples were measured in both three-electrode system and supercapacitor cell. For the preparation of working electrode, 80 wt % electroactive material, 10 wt % polytetrafluoroethylene (PTFE) binder, and 10 wt % acetylene black were mixed in the ethanol. Then, the slurry of the above mixture was blended thoroughly for 20 min and dried at 80 °C for 8 h in air to evaporate the ethanol, then the mixture was rolled into 100–120 μm thick films by a roller press. After dried at 105 °C for 10 h, the thick film was punched by a punching machine with the punch diameter of 1.2 cm, then a disk-like film (1.13 cm^2) was taken out and mechanically pressed onto the nickel foam with the help of roller press. The electrochemical testing was carried out on a CHI660E electrochemical working station (Shanghai Chenhua Instrument, Inc., China) with 6.0 M KOH as the aqueous electrolyte in a three-electrode system. The Pt plate (2 cm × 2 cm) electrode was used as the counter electrode, while the Hg/HgO electrode as the reference electrode. The cyclic voltammetry (CV) and galvanostatic charging/discharging (GCD) techniques were conducted to probe the electrochemical performances of the $Ni(OH)_2$ electrodes. Finally, the cycle life measurements were performed on a LAND battery test system. The specific capacitance of the single electrode was calculated according to the following equation [21]:

$$C_s = \frac{I\Delta t}{m\Delta V} \tag{1}$$

Where C_s (F g^{-1}) is the specific capacitance of the electrode, I (A) is the discharge current, Δt (s) is the discharge time, and m (g) is the mass of the active material in the working electrode, and ΔV (V) is the voltage range.

The hybrid supercapacitors were constructed in a coin cell with two different working electrodes using $Ni(OH)_2$ as the positive electrode material, hierarchically porous carbon (HPC) as the negative electrode material, a cellulose separator, and 6 M KOH aqueous electrolyte. The HPC was synthesized according to the report published by our group before [22] and the preparation of the negative electrode was similar to that of positive electrode, which was described above. The loading mass of the active material in negative and positive electrodes was estimated as follows [23]:

$$\frac{m_+}{m_-} = \frac{C_- \times V_-}{C_+ \times V_+} \tag{2}$$

Where the m_+ and m_- are the mass of active materials in positive and negative electrodes, respectively; C_+ and C_- are the specific capacitances of active materials in positive and negative electrodes, respectively; and the V_+ and V_- are the potential windows of the positive and negative electrodes, respectively.

The electrochemical performances of the supercapacitor cell were also determined by CV and GCD. For the hybrid supercapacitor, its specific capacitance (C) can be evaluated according to the following equation [21]:

$$C = \frac{I\Delta t}{M\Delta V} \tag{3}$$

Where M (g) refers to the total mass of active materials on both electrodes. The energy and power densities were evaluated based on the following equations [24,25]:

$$E = 0.5 \times C \times \Delta V^2 \tag{4}$$

$$P = \frac{E}{\Delta t} \tag{5}$$

Where E (W h kg^{-1}) is the energy density, C (F g^{-1}) is the specific capacitance of the device, ΔV (V) is the cell voltage, P (W kg^{-1}) is the power density, and Δt (s) is the discharge time. The detailed unit calculation of energy density and power density is shown in the Supplementary Materials.

3. Results and discussion

Fig. 1b illustrates the schematic diagram of the formation process of the 3D porous flower-like $Ni(OH)_2$. The main design thought is that the $Ni(OH)_2$ nuclei firstly grow into tiny nanoparticles which aggregate and grow into preferentially the petal-like nanosheets because of its brucite-like crystal structure [26], simultaneously, the petals interconnect with each other and self-assemble into the flower-like $Ni(OH)_2$ with an open porous structure by aggregative growths [26,27]. The microstructure and morphology of the $Ni(OH)_2$ obtained at 100–300 °C with different magnifications were characterized with the aid of SEM. As presented in Fig.S1, the $Ni(OH)_2$ consists of many homogeneous dispersive particles with the size around 1–2 μm. After enlarging the magnification (Fig. 1c), it can be clearly observed that the morphology of $Ni(OH)_2$ is flower-like architecture with several tens of order-attached petal-like nanosheets. Notably, these curved nanosheets are interconnected with each other, which is beneficial for electrolyte ions diffusion during the electrochemical process. With treatment temperature increasing, the products almost maintain the original 3D porous structure with petal-like nanosheets (Fig. 1c–g). Nevertheless, the color of all samples changes obviously, from light green into black, as shown in the lower right corner of Fig. 1c–g. The detailed morphological and structural information of $Ni(OH)_2$ are further

obtained with the help of TEM and HRTEM. As exhibited in Fig. 1h and i, the product obtained at 100 °C presents an irregular flower-like morphology, and is constituted by numerous interconnected nanosheets which are curved and overlapped with ultrathin thickness, which confirms the results of SEM observations. Further enlargement (Fig. 1j) presents that the individual nanosheet consists of numerous spherical nanoparticles with inhomogeneous size of several nanometers. Thus, the 3D flower-like $Ni(OH)_2$ presents a hierarchical porous structure, which includes the ultrathin nanosheets as the second grade and nanoparticles as the third grade. The HRTEM image (Fig. 1k) shows the distinct lattice spacing of about 0.230 nm, which is in agreement with the (015) interplanar distance of the hexagonal phase of $Ni(OH)_2$.

The X-ray diffraction (XRD) patterns of the five products prepared at different conditions are exhibited in Fig. 2a. For the Sample-100, the peaks located at $2\theta = 16.2°$, 33.3°, 38.5°, 51.9°, 59.2°, 62.6°, 69.6°, and 73° are attributed to the (001), (100), (101), (102), (110), (111), (103), and (201) lattice planes of brucite-like hexagonal β-$Ni(OH)_2$ phase (JCPDS card No. 14–0117), respectively [28]. More than that, the peaks located at 12.4° and 21.7° are also scanned out, which correspond to the (003) and (006) facets of the α-$Ni(OH)_2$ phase (JCPDS card No. 38–0715) [12], respectively, which demonstrates that α and β phases coexist in the Sample-100. Moreover, it is notable that there are no other peaks detected, suggesting the nature of $Ni(OH)_2$, even though two phases coexist. With increasing the temperature, the intensities of characteristic peaks of β-phase $Ni(OH)_2$ have no significant change; nevertheless, the peak intensities of α-$Ni(OH)_2$ gradually weaken, indicating the reduction of α-$Ni(OH)_2$ (Fig. S2a). Importantly, the rising of temperature makes the main diffraction peaks of $Ni(OH)_2$ shift to lower angles (Fig. S2b), indicating that the interlayer spacing of $Ni(OH)_2$ broadens, which facilitates fast ions diffusion within the active materials [29]. When the calcination temperature rises to 300 °C, the characteristic peaks of $Ni(OH)_2$ have completely disappeared. For the Sample-300, the main peaks observed at $2\theta = 37.2°$, 43.3°, 62.7°, 75.2°, and 79.2°correspond to the (110), (200), (220), (311) and (222) crystal planes of cubic NiO phase (JCPDS card No. 4–0835), indicating that both the α-$Ni(OH)_2$ and β-$Ni(OH)_2$ have totally converted into NiO at 300 °C.

The FTIR spectrum of the Sample-100 is shown in Fig. 2b. The sharp peak located at around 3632 cm^{-1} and the broad peak around 3437 cm^{-1} are both assigned to the hydrogen-bonded O–H stretching vibration [30–32]. The weak band at 2911 cm^{-1} can be ascribed to the $-CH_x$ groups, while the band at 2180 cm^{-1} confirms the presence of the intercalated C–O species in nickel hydroxide [33], which are probably from the solvent and incompletely eliminated during the washing stage [34]. The peak around 1633 cm^{-1} is ascribed to the bending vibration of O–H in the weakly absorbed water molecules on 3D structure surface of $Ni(OH)_2$ [9,35]. The peak observed at 1376 cm^{-1} is owing to the vibration of carbonate ion, which is mainly coming from the absorption of atmospheric CO_2 during the synthesis [9,36,37]. The peak at 617 cm^{-1} is attributed to the lattice vibration of O–H [34], and two peaks centered at 519 and 458 cm^{-1} correspond to the bending vibration of Ni–O–H and stretching vibration of Ni–O, respectively [34]. These results indicate that the product possesses the $Ni(OH)_2$ structure.

In order to further confirm the product composition, the X-ray photoelectron spectroscopy (XPS) has been adopted and the results are shown in Fig. 2c–d. The XPS survey spectrum of Sample-100 (Fig. 2c) confirms the existence of the carbon, oxygen, and nickel

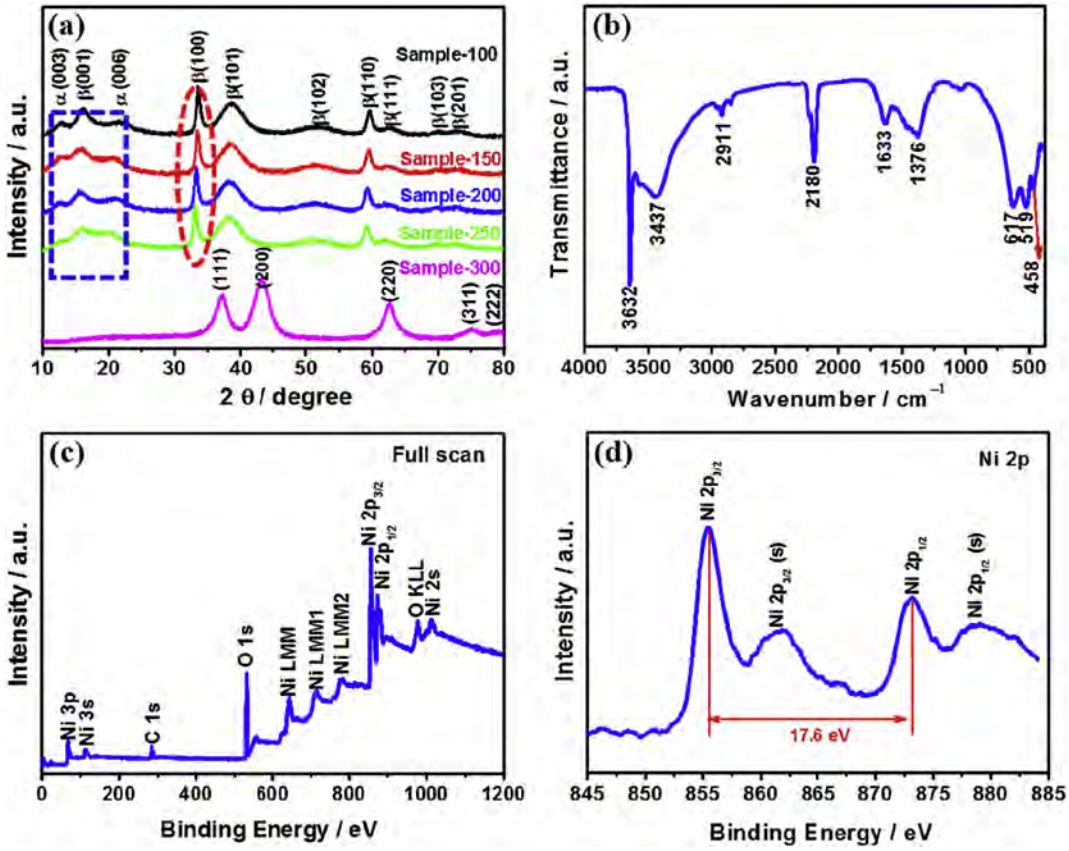

Fig. 2. (a) XRD spectra of the Sample-100, Sample-150, Sample-200, Sample-250, and Sample-300; (b) FTIR curve, (c) XPS survey spectrum, and (d) Ni 2p spectrum of the Sample-100.

elements in the sample. Among them, the oxygen and nickel elements come from $Ni(OH)_2$, while the carbon element is from the solvent. The high resolution Ni 2p XPS spectrum (Fig. 2d) exhibits two characteristic peaks of Ni $2p_{3/2}$ and Ni $2p_{1/2}$ which are located at 855.5 and 873.1 eV, respectively, with a spin-energy separation of 17.6 eV, indicating the characteristic of $Ni(OH)_2$ phase [28,38,39]. The two satellite peaks at about 862 and 879 eV are observed, which correspond to Ni $2p_{3/2}$ and Ni $2p_{1/2}$, respectively. Moreover, the FTIR curve and XPS survey spectrum of Sample-300 with detailed analysis are shown in Fig. S3, confirming the NiO nature of Sample-300.

The nitrogen adsorption/desorption isotherms of $Ni(OH)_2$ samples (excluding the NiO sample) were conducted to obtain their specific surface areas and pore structures which are closely related with the electrochemical properties of $Ni(OH)_2$, as shown in Fig. 3. All isotherms with an evident hysteresis loop in the range of 0.45–0.98 P/P_0 should be categorized to type IV based on the IUPAC classification, implying the capillary condensation taking place in the mesopores inside the $Ni(OH)_2$ samples [22,40]. The BET specific surface areas of the products are 61.5, 69.9, 77.3, and 79.4 $m^2 g^{-1}$ with the pore volumes of 0.157, 0.146, 0.155, and 0.16 $cm^3 g^{-1}$ for Sample-100, Sample-150, Sample-200, and Sample-250, respectively. The increase of the specific surface areas along with rising temperature is attributed to the gradual removal of chemically attached water in the nickel hydroxide and formation of more open structure during the water vapor scape when the temperature rises, as inferred from the TG analysis (Fig. S4). The Sample-250 exhibits the highest specific surface area and largest pore volume, being beneficial for the improvement of electrochemical properties. Notably, the specific surface area of Sample-250 is larger than that of other $Ni(OH)_2$ reported previously [6,17,35,41,42]. As shown in the insets, the pore size distributions of all $Ni(OH)_2$ samples show a wide pore size in the range of 0.8–33 nm, indicating the coexistence of micropore and mesopore, further confirming their hierarchical porous structures.

The electrochemical performances of all $Ni(OH)_2$ samples are first investigated in three-electrode configuration. The typical cyclic voltammetry (CV) curves of the four $Ni(OH)_2$ samples in the voltage range of 0–0.55 V at the scan rate of 5 mV s^{-1} are exhibited in Fig. 4a. Apparently, all CV curves share the similar shapes, and show a pair of redox peaks, clearly suggesting the intrinsic pseudocapacitance behavior of these battery-type electrodes [43], which mainly comes from the faradaic redox reactions happening in this system. The α-$Ni(OH)_2$ exists unstably and quickly transforms into β-$Ni(OH)_2$ phase under strong alkaline electrolyte [9], hence, the redox peaks are mainly attributed to the transformation between the β-$Ni(OH)_2$ and β-NiOOH based on the equation as follows [44,45]:

$$\beta\text{-}Ni(OH)_2 + OH^- \leftrightarrow \beta\text{-}NiOOH + H_2O + e^- \quad (6)$$

Obviously, the Sample-250 shows the largest current response and integral area among these samples, suggesting the highest specific capacitance of Sample-250. The GCD measurements were also conducted to reveal the electrochemical properties of $Ni(OH)_2$ samples. As displayed in Fig. 4b, the distinct voltage plateaus can be observed in the discharge process, further supporting their typical pseudocapacitance nature [43], which is consistent fine with the results of CV tests. The specific capacitances of Sample-100, Sample-150, Sample-200, and Sample-250 are calculated to be 1798, 1963, 2081, and 2110 F g^{-1} at 1.0 A g^{-1}, respectively, according to the GCD curves. Obviously, both measurements manifest that the Sample-250 possesses the highest specific capacitance among these samples. This result can be attributed to that: (i) With the

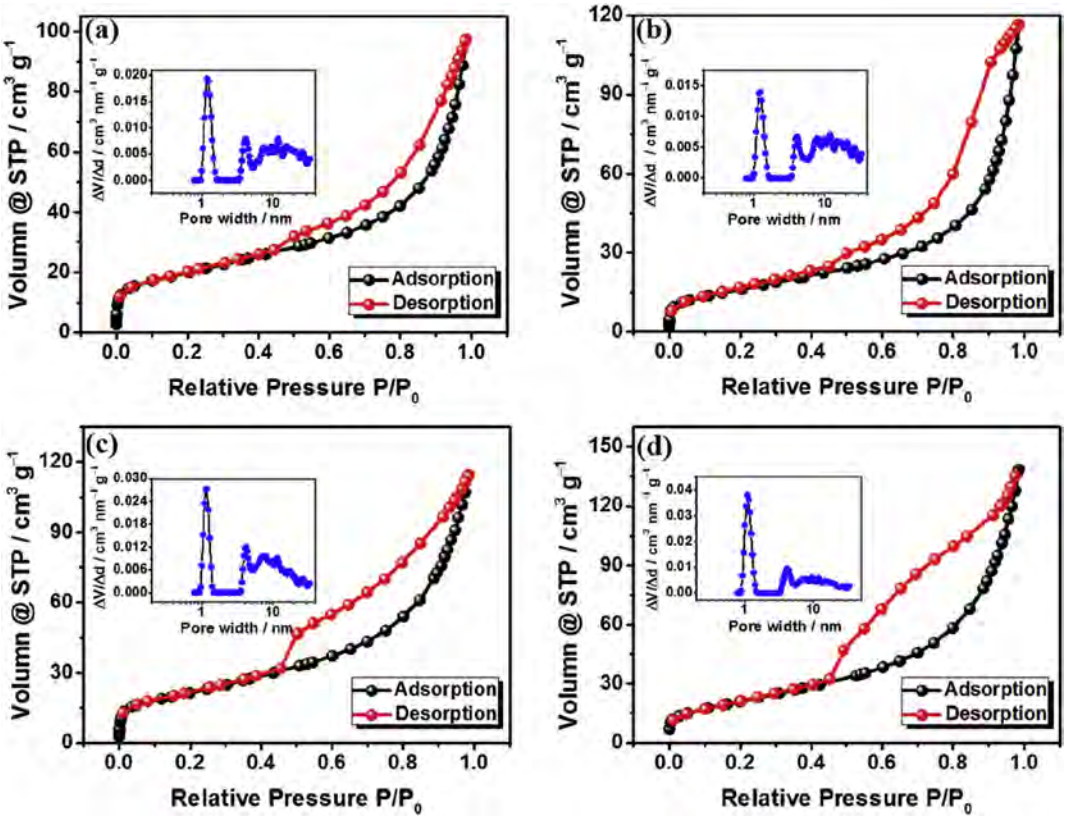

Fig. 3. Nitrogen adsorption/desorption isotherms and pore size distribution curves (inset) of (a) Sample-100, (b) Sample-150, (c) Sample-200, and (d) Sample-250.

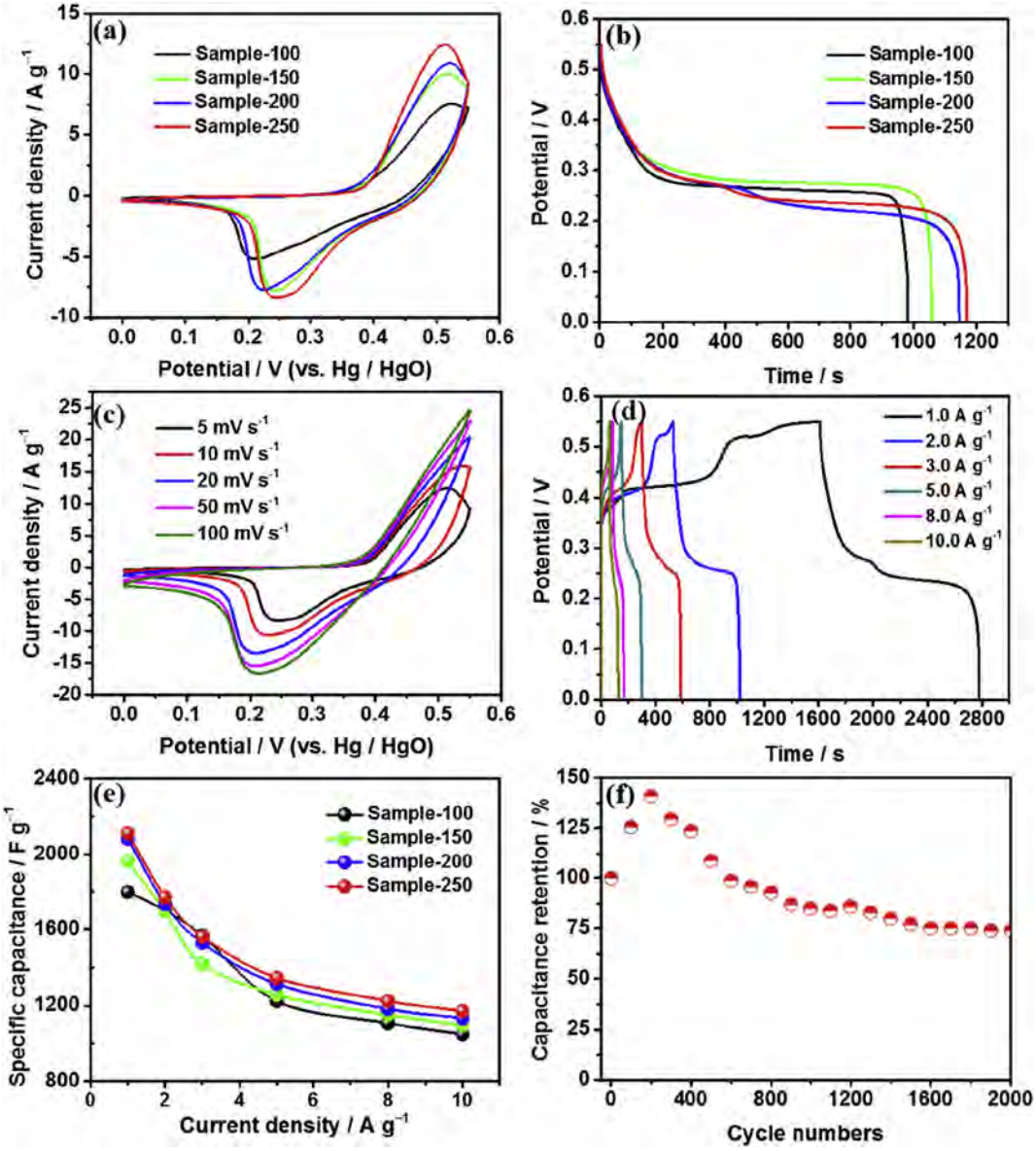

Fig. 4. Electrochemical performances of the $Ni(OH)_2$ samples measured in three-electrode system: (a) CV curves of Sample-100, Sample-150, Sample-200, and Sample-250; (b) Discharging curves of Sample-100, Sample-150, Sample-200, and Sample-250 at the current density of 1.0 A g^{-1}; (c) CV curves of the Sample-250 at various scan rates of 5–100 mV s^{-1}; (d) GCD curves for Sample-250 at various current densities of 1.0–10.0 A g^{-1}; (e) Comparison of the rate performance for Sample-100, Sample-150, Sample-200, and Sample-250 as a function of current density; (f) Cycle performance of Sample-250 over 2000 cycles at 5.0 A g^{-1}.

rising of the calcination temperature, the specific surface area of the product gradually increases, which promotes the more electrolyte access within the porous nanostructure and provides more efficient active sites for electrolyte; the open structure formed because of the water vapor scape during the calcination process gradually increases, which enables the faster ion transport within the active materials; the interlayer spacing within crystal structure gradually enlarges, which favors the ions diffusion and electron transportation within the active materials. Hence, capacitance of the samples presents the general improvement with rising temperature. (ii) Among these four samples, the Sample-250 is obtained at the highest temperature and possesses the largest specific surface area, the most open structure, and largest interlayer spacing within crystal structure, therefore, Sample-250 shows the best electrochemical performance.

To investigate the detailed electrochemical performance of the Sample-250, systematic electrochemical measurements were carried out. Fig. 4c depicts the CV curves of Sample-250 at the scan rates of 5–100 mV s^{-1} with a voltage range of 0–0.55 V. The non-rectangular shapes of the CV curves signify that the charge storage of Sample-250 is a pseudocapacitance process which originates from the faradaic reaction [46]. It can be found that the cathodic peaks gradually shift to the lower potentials with the rising of scan rate, possibly owing to the polarization of the electrode [47]. The GCD curves of Sample-250 at the current densities of 1.0, 2.0, 3.0, 5.0, 8.0, and 10.0 A g^{-1} are shown in Fig. 4d. All charge-discharge curves present the obvious voltage plateaus, further exhibiting typical pseudocapacitance behavior of battery-type electrode, which is consistent with CV behavior. The specific capacitances of all $Ni(OH)_2$ samples derived from their GCD curves (Fig. S5) and the data are presented in Fig. 4e. Impressively, the $Ni(OH)_2$ obtained at 250 °C delivers the specific capacitances of 2110, 1771, 1564, 1346, 1224, and 1171 F g^{-1} at current densities of 1.0, 2.0, 3.0, 5.0, 8.0, and 10.0 A g^{-1}, respectively, which are higher than those values of other

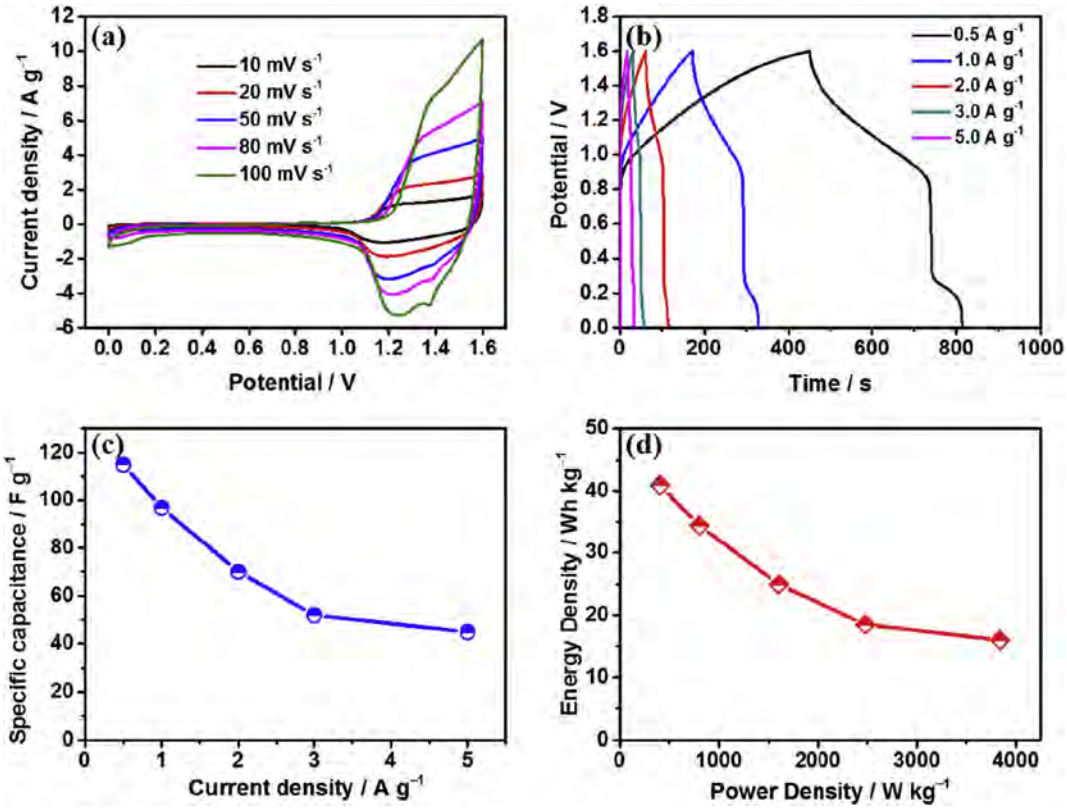

Fig. 5. Electrochemical performances of the as-fabricated $Ni(OH)_2$//HPC hybrid supercapacitor: (a) CV curves at the scan rates of 10–100 mV s^{-1}; (b) GCD curves at the current densities of 0.5–5.0 A g^{-1}; (c) the corresponding specific capacitances as a function of current density; (d) the Ragone plots for as-fabricated $Ni(OH)_2$//HPC hybrid supercapacitor.

$Ni(OH)_2$ samples, in consistent with the CV measurements (Fig. S6). Moreover, the specific capacitance of Sample-250 at 1.0 A g^{-1} is also considerably superior to other nickel hydroxide, nickel-cobalt hydroxide or $Ni(OH)_2$/carbon-based composite materials reported previously (Table S1). Compared with those $Ni(OH)_2$ reported previously, the higher specific capacitance of the Sample-250 may be ascribed to (i) its 3D flower-like structure with interconnected network which offers superior electron transportation property, shorter ion-diffusion pathway and larger space for electrolyte easy access towards the whole structure, and (ii) its hierarchical porous architecture which facilitates faster ion diffusion and provides higher specific surface area and more active area for high-efficiency use of the active materials, from the above, thus improving its total capacitance. The cycle stability of Sample-250 was evaluated by the capacitance retention at the current density of 5.0 A g^{-1}. As shown in Fig. 4f, the specific capacitance increases initially, which is ascribed to that the electrode material generates large volume changes after repeating charging/discharging process and then becomes more open-structured and more accessible to the electrolyte. Consequently, more active materials are involved and contribute to the specific capacitance. Then, the specific capacitance starts to decline after 200 cycles and holds 53% of the maximum specific capacitance over 2000 cycles, suggesting a moderate cycle stability. The capacitance loss is probably owning to the serious agglomeration and volume change of the active material in the cycle process. Due to the NiO nature of Sample-300, the electrochemical performance (specific capacitance of 316 F g^{-1} at 0.5 A g^{-1}) of Sample-300 is not discussed in detail as well as in comparison of $Ni(OH)_2$ samples in the main text, but presented in Fig. S7.

To evaluate the practical potential of as-synthesized $Ni(OH)_2$, an hybrid supercapacitor was assembled with Sample-250 as the positive electrode and HPC as the negative electrode. The detailed electrochemical performance of hierarchically porous carbons is presented in Fig. S8. As exhibited in Fig. 5a, it is interesting to note that the $Ni(OH)_2$//HPC hybrid supercapacitor has a stable electrochemical window up to 1.6 V. An obvious redox peak can be clearly observed in the CV curves, indicating the pseudocapacitive property of the $Ni(OH)_2$//HPC hybrid supercapacitor, which is contributed by the positive electrode. Along with the scan rate increasing, the shapes of CV curves maintain well and the redox peaks shift mildly to a more negative or positive position. The Fig. 5b shows the GCD curves of $Ni(OH)_2$//HPC hybrid supercapacitor at different current densities of 0.5–5.0 A g^{-1}. The corresponding specific capacitances calculated according to the GCD curves are shown in Fig. 5c. The specific capacitances of the device are 115, 97, 70, 52, and 45 F g^{-1} at the current densities of 0.5, 1.0, 2.0, 3.0, and 5.0 A g^{-1}, respectively, which is higher or comparable to the data reported previously [23,30,48]. The Ragone plot revealing the relationship between the energy density and power density of the hybrid supercapacitor is exhibited in Fig. 5d. The energy density of 40.9 W h kg^{-1} can be achieved at a power density of 0.405 kW kg^{-1}, and an energy density of 16 W h kg^{-1} at the power density of 3.84 kW kg^{-1}. These results are superior to some asymmetric supercapacitors reported previously, including $Ni(OH)_2$//NTAC (32.7 W h kg^{-1} at 71.5 W kg^{-1}) [48], $Ni(OH)_2$//AC (12.6 W h kg^{-1} at 1.67 kW kg^{-1}) [23], AC//β-$Ni(OH)_2$ (36.2 W h kg^{-1} at 0.1 kW kg^{-1}) [49], NCOH//AC (19.2 W h kg^{-1} at 80.5 W kg^{-1}) [30], AC//MnO_2 (21 W h kg^{-1} at 0.3 kW kg^{-1}) [50], NiO//AC (7–15 W h kg^{-1}) [51], NiO//AC (6–20 W h kg^{-1}) [52], and comparable to rGONF/$Ni(OH)_2$//AC (44.1 W h kg^{-1} at 0.467 kW kg^{-1}) [53]. The high energy density of this device is ascribed to the excellent capacitance properties of Sample-250 (2110 F g^{-1} at 1.0 A g^{-1}), hierarchically porous carbons (296 F g^{-1} at 1.0 A g^{-1}), and high potential window (1.6 V)

according to equation (4). Hence, the superior energy density provided by the as-fabricated $Ni(OH)_2$//HPC hybrid supercapacitor makes it possible in practical application in the area of highly promising energy-storage devices.

4. Conclusion

To summarize, we creatively sythesized a self-assembly 3D porous flower-like nickel hydroxide by a solution-based solvothermal-precipitation method under the simple, cost-effective, and environmentally friendly condition. A series of $Ni(OH)_2$ products with unique features obtained under different conditions were prepared and characterized systematically. The optimized $Ni(OH)_2$ product shows the high specific capacitances of 2110 and 1171 F g^{-1} at 1.0 and 10.0 A g^{-1}, respectively, as well as a moderate cycle stability with 53% of the maximum specific capacitance over 2000 cycles at 5.0 A g^{-1}. When the Sample-250 is applied as the positive eletrode material with the hierarchically porous carbons as the negative electrode material in hybrid supercapacitor, a high specific capacitance of 115 F g^{-1} is achieved. The hybrid supercapacitor can be operated at a stable electrochemical window up to 1.6 V and deliver a high energy density of 40.9 W h kg^{-1} at the power density of 405 W kg^{-1}. The electrochemical performance measurements prove the potential of 3D porous $Ni(OH)_2$ with flower-like structure in the high-performance hybrid supercapacitor. Furthermore, the solvothermal-precipitation method provides an effective self-assembly route to fabricate not just $Ni(OH)_2$ but various metallic oxides/hydroxides with excellent performance for advanced energy-storage systems.

Acknowledgements

This work was financially supported by the Independent Research Project of State Key Laboratory of Traction Power (No. 2017TPL_Z04, 2016TPL_Z03); the Fundamental Research Funds for the Central Universities of China (2682016ZY01 and 2682017ZDPY01); the scientific and technological projects for Distinguished Young Scholars of Sichuan Province (No.2015JQ0013); the National Natural Science Foundation of China (No. 51602265); and China Postdoctoral Science Foundation (2016M592692).

Appendix A. Supplementary data

Supplementary data related to this article can be found at https://doi.org/10.1016/j.electacta.2018.02.130.

References

[1] Y. Wang, S. Gai, N. Niu, F. He, P. Yang, Fabrication and electrochemical performance of 3D hierarchical β-$Ni(OH)_2$ hollow microspheres wrapped in reduced graphene oxide, J. Mater. Chem. 1 (2013) 9083.
[2] J. Gou, S. Xie, Y. Liu, C. Liu, Flower-like nickel-cobalt hydroxides converted from phosphites for high rate performance hybrid supercapacitor electrode materials, Electrochim. Acta 210 (2016) 915.
[3] Y. Wang, Y. Song, Y. Xia, Electrochemical capacitors: mechanism, materials, systems, characterization and applications, Chem. Soc. Rev. 45 (2016) 5925.
[4] L. Zhang, H.T. Zhang, L. Jin, B.B. Zhang, F.Y. Liu, H. Su, F.J. Chun, Q.H. Li, J.F. Peng, W.Q. Yang, Composition controlled nickel cobalt sulfide core-shell structures as high capacity and good rate-capability electrodes for hybrid supercapacitors, RSC Adv. 6 (2016) 50209.
[5] Z. Lu, Z. Chang, W. Zhu, X. Sun, Beta-phased $Ni(OH)_2$ nanowall film with reversible capacitance higher than theoretical faradic capacitance, Chem. Commun. 47 (2011) 9651.
[6] Y. Wang, S. Gai, C. Li, F. He, M. Zhang, Y. Yan, P. Yang, Controlled synthesis and enhanced supercapacitor performance of uniform pompon-like β-$Ni(OH)_2$ hollow microspheres, Electrochim. Acta 90 (2013) 673.
[7] T. Brousse, D. Bélanger, J. Long, To be or not to be peudocapacitive? J. Electrochem. Soc. 162 (2015). A5185.
[8] L. Kumari, W.Z. Li, Self-assembly of β-$Ni(OH)_2$ nanoflakelets to form hollow submicrospheres by hydrothermal route, Physica E 41 (2009) 1289.
[9] H. Li, S. Liu, C. Huang, Z. Zhou, Y. Li, D. Fang, Characterization and supercapacitor application of coin-like β-nickel hydroxide nanoplates, Electrochim. Acta 58 (2011) 89.
[10] C.-W. Kung, Y.-H. Cheng, K.-C. Ho, Single layer of nickel hydroxide nanoparticles covered on a porous Ni foam and its application for highly sensitive non-enzymatic glucose sensor, Sens. Actuators, B 204 (2014) 159.
[11] W. Liu, C. Ju, D. Jiang, L. Xu, H. Mao, K. Wang, Ionic liquid-assisted grown of beta-nickel hydroxide nanowires on reduced graphene oxide for high-performance supercapacitors, Electrochim. Acta 143 (2014) 135.
[12] J. Huang, T. Lei, X. Wei, X. Liu, T. Liu, D. Cao, J. Yin, G. Wang, Effect of Al-doped β-$Ni(OH)_2$ nanosheets on electrochemical behaviors for high performance supercapacitor application, J. Power Sources 232 (2013) 370.
[13] X. Zang, C. Sun, Z. Dai, J. Yang, X. Dong, Nickel hydroxide nanosheets supported on reduced graphene oxide for high-performance supercapacitors, J. Alloy. Comp. 691 (2017) 144.
[14] T. Taşköprü, M. Zor, E. Turan, Structural characterization of nickel oxide/hydroxide nanosheets produced by CBD technique, Mater. Res. Bull. 70 (2015) 633.
[15] G. Nagaraju, S.M. Cha, J.S. Yu, Ultrathin nickel hydroxide nanosheet arrays grafted biomass-derived honeycomb-like porous carbon with improved electrochemical performance as a supercapacitive material, Sci. Rep. 7 (2017) 45201.
[16] F. Nekouei, H. Kargarzadeh, S. Nekouei, I. Tyagi, S. Agarwal, V. Kumar Gupta, Preparation of Nickel hydroxide nanoplates modified activated carbon for Malachite Green removal from solutions: kinetic, thermodynamic, isotherm and antibacterial studies, Process Saf. Environ. Protect. 102 (2016) 85.
[17] H. Jiang, T. Zhao, C. Li, J. Ma, Hierarchical self-assembly of ultrathin nickel hydroxide nanoflakes for high-performance supercapacitors, J. Mater. Chem. 21 (2011) 3818.
[18] X. Zhu, Y. Zhong, H. Zhai, Z. Yan, D. Li, Nanoflake nickel hydroxide and reduced graphene oxide composite as anode materials for high capacity lithium ion batteries, Electrochim. Acta 132 (2014) 364.
[19] Y.F. Yuan, X.H. Xia, J.B. Wu, J.L. Yang, Y.B. Chen, S.Y. Guo, Nickel foam-supported porous $Ni(OH)_2$/NiOOH composite film as advanced pseudocapacitor material, Electrochim. Acta 56 (2011) 2627.
[20] D. Wang, C. Song, Z. Hu, X. Fu, Fabrication of hollow spheres and thin films of nickel hydroxide and nickel oxide with hierarchical structures, J. Phys. Chem. B 109 (2005) 1125.
[21] S. Li, C. Yu, J. Yang, C. Zhao, M. Zhang, H. Huang, Z. Liu, W. Guo, J. Qiu, A superhydrophilic “nanoglue” for stabilizing metal hydroxides onto carbon materials for high-energy and ultralong-life asymmetric supercapacitors, Energy Environ. Sci. 10 (2017) 1958.
[22] H.T. Zhang, L. Zhang, J. Chen, H. Su, F.Y. Liu, W.Q. Yang, One-step synthesis of hierarchically porous carbons for high-performance electric double layer supercapacitors, J. Power Sources 315 (2016) 120.
[23] H.B. Li, M.H. Yu, F.X. Wang, P. Liu, Y. Liang, J. Xiao, C.X. Wang, Y.X. Tong, G.W. Yang, Amorphous nickel hydroxide nanospheres with ultrahigh capacitance and energy density as electrochemical pseudocapacitor materials, Nat. Commun. 4 (2013) 1894.
[24] H. Chen, L. Hu, M. Chen, Y. Yan, L. Wu, Nickel-cobalt layered double hydroxide nanosheets for high-performance supercapacitor electrode materials, Adv. Funct. Mater. 24 (2014) 934.
[25] N. Choudhary, C. Li, J. Moore, N. Nagaiah, L. Zhai, Y. Jung, J. Thomas, Asymmetric supercapacitor electrodes and devices, Adv. Mater. 29 (2017) 1605336.
[26] S. Zhang, H.C. Zeng, Self-assembled hollow spheres of β-$Ni(OH)_2$ and their derived nanomaterials, Chem. Mater. 21 (2009) 871.
[27] M. Cao, X. He, J. Chen, C. Hu, Self-assembled nickel hydroxide three-dimensional nanostructures: a nanomaterial for alkaline rechargeable batteries, Cryst. Growth Des. 7 (2007) 170.
[28] G. Zu, J. Shen, Z. Zhang, B. Zhou, X. Wang, G. Wu, Y. Zhang, Homogeneous deposition of $Ni(OH)_2$ onto cellulose-derived carbon aerogels for low-cost energy storage electrodes, RSC Adv. 7 (2017) 10583.
[29] H. Chen, L. Hu, Y. Yan, R. Che, M. Chen, L. Wu, One-step fabrication of ultrathin porous nickel hydroxide-manganese dioxide hybrid nanosheets for supercapacitor electrodes with excellent capacitive performance, Adv. Energy Mater 3 (2013) 1636.
[30] Y. Tang, Y. Liu, S. Yu, W. Guo, S. Mu, H. Wang, Y. Zhao, L. Hou, Y. Fan, F. Gao, Template-free hydrothermal synthesis of nickel cobalt hydroxide nanoflowers with high performance for asymmetric supercapacitor, Electrochim. Acta 161 (2015) 279.
[31] Y. Li, J. Yao, Y. Zhu, Z. Zou, H. Wang, Synthesis and electrochemical performance of mixed phase α/β nickel hydroxide, J. Power Sources 203 (2012) 177.
[32] M. Sebastian, C. Nethravathi, M. Rajamathi, Interstratified hybrids of α-hydroxides of nickel and cobalt as supercapacitor electrode materials, Mater. Res. Bull. 48 (2013) 2715.
[33] Z. Zhu, N. Wei, H. Liu, Z. He, Microwave-assisted hydrothermal synthesis of $Ni(OH)_2$ architectures and their in situ thermal convention to NiO, Adv. Powder Technol. 22 (2011) 422.
[34] M. Wang, Y. Ni, L. Cao, D. Zhao, X. Ma, Porous Ni/beta-$Ni(OH)_2$ superstructures: rapid solvothermal synthesis, characterization, and electrochemical property, J. Colloid Interface Sci. 401 (2013) 8.
[35] Q. Li, H. Ni, Y. Cai, X. Cai, Y. Liu, G. Chen, L.-Z. Fan, Y. Wang, Preparation and supercapacitor application of the single crystal nickel hydroxide and oxide nanosheets, Mater. Res. Bull. 48 (2013) 3518.

[36] H. Zhou, J. Peng, X. Qiu, Y. Gao, L. Lu, W. Wang, β-Ni(OH)2 nanosheets: an effective sensing platform for constructing nucleic acid-based optical sensors, J. Mater. Chem. B 5 (2017) 7426.
[37] T. Meng, P.-P. Ma, J.-L. Chang, Z.-H. Wang, T.-Z. Ren, The electrochemical capacitive behaviors of NiO nanoparticles, Electrochim. Acta 125 (2014) 586.
[38] K. Wang, X. Zhang, X. Zhang, D. Chen, Q. Lin, A novel $Ni(OH)_2$/graphene nanosheets electrode with high capacitance and excellent cycling stability for pseudocapacitors, J. Power Sources 333 (2016) 156.
[39] R. Yuksel, S. Coskun, Y.E. Kalay, H.E. Unalan, Flexible, silver nanowire network nickel hydroxide core-shell electrodes for supercapacitors, J. Power Sources 328 (2016) 167.
[40] K.S.W. Sing, D.H. Everett, L.M.R.A.W. Haul, R.A. Pierotti, J. Rouquerol, T.Siemieniewska, Reporting physisorption data for gas/solid systems with special reference to the determination of surface area and porosity, Pure Appl. Chem. 54 (1982) 2201.
[41] D.P. Dubal, V.J. Fulari, C.D. Lokhande, Effect of morphology on supercapacitive properties of chemically grown β-$Ni(OH)_2$ thin films, Microporous Mesoporous Mater. 151 (2012) 511.
[42] Z. Li, W. Zhang, Y. Su, Z. Li, J. Groeper, Self-assembling $Ni(OH)_2$/alpha-Fe_2O_3 composites for pseudocapacitors with excellent electrochemical performance, Nanotechnology 28 (2017) 045603.
[43] Y. Guo, L. Yu, C.-Y. Wang, Z. Lin, X.W.D. Lou, Hierarchical tubular structures composed of Mn-based mixed metal oxide nanoflakes with enhanced electrochemical properties, Adv. Funct. Mater. 25 (2015) 5184.
[44] P. Oliva, J. Leonardi, J.F. Laurent, Review of the structure and the electrochemistry of nickel hydroxides and oxy-hydroxides, J. Power Sources 8 (1982) 229.
[45] R.E. Carbonio, V.A. Macagno, M.C. Giordano, J.R. Vilche, A.J. Arvía, A transition in the kinetics of the $Ni(OH)_2$/NiOOH electrode reaction, Electrochem. Soc. 129 (1982) 983.
[46] F.Y. Liu, B.B. Zhang, H. Su, H.T. Zhang, L. Zhang, W.Q. Yang, Controllable synthesis of self-assembly Co_3O_4 nanoflake microspheres for electrochemical performance, Nanotechnology 27 (2016), 355603.
[47] W.L. Yang, Z. Gao, J. Ma, J. Wang, B. Wang, L.H. Liu, Effects of solvent on the morphology of nanostructured Co_3O_4 and its application for high-performance supercapacitors, Electrochim. Acta 112 (2013) 378.
[48] Y. Tang, Y. Liu, S. Yu, Y. Zhao, S. Mu, F. Gao, Hydrothermal synthesis of a flower-like nano-nickel hydroxide for high performance supercapacitors, Electrochim. Acta 123 (2014) 158.
[49] J. Huang, P. Xu, D. Cao, X. Zhou, S. Yang, Y. Li, G. Wang, Asymmetric supercapacitors based on β-$Ni(OH)_2$ nanosheets and activated carbon with high energy density, J. Power Sources 246 (2014) 371.
[50] C. Xu, H. Du, B. Li, F. Kang, Y. Zeng, Asymmetric activated carbon-manganese dioxide capacitors in mild aqueous electrolytes containing alkaline-earth cations, J. Electrochem. Soc. 156 (2009). A435.
[51] D.-W. Wang, F. Li, H.-M. Cheng, Hierarchical porous nickel oxide and carbon as electrode materials for asymmetric supercapacitor, J. Power Sources 185 (2008) 1563.
[52] H. Inoue, Y. Namba, E. Higuchi, Preparation and characterization of Ni-based positive electrodes for use in aqueous electrochemical capacitors, J. Power Sources 195 (2010) 6239.
[53] C. Zhang, Q. Chen, H. Zhan, Supercapacitors based on reduced graphene oxide nanofibers supported $Ni(OH)_2$ nanoplates with enhanced electrochemical performance, ACS Appl. Mater. Interfaces 8 (2016) 22977.